Journal of Membrane Science 669 (2023) 121328

Contents lists available at ScienceDirect

Journal of Membrane Science

journal homepage: www.elsevier.com/locate/memsci

Preactivated zeolite nanosheet plate-tiled membrane on porous PVDF film: Synthesis and study of proton-selective ion conduction

Landysh Iskhakova, Zishu Cao, Xinhui Sun, Jan Gabski, Junhang Dong *

Department of Chemical and Environmental Engineering, University of Cincinnati, Cincinnati, OH, 45221, USA

ARTICLE INFO

Keywords:
Zeolite nanosheet
Membrane
Polymer support
Ion separator
Redox flow battery

ABSTRACT

Preactivated MFI zeolite nanosheet plates (ZNPs) with large areas (~2.0 × 2.0 μm^2) and nanometer thicknesses (~60 nm) were prepared directly in liquid-dispersed state. The individual ZNP was a stack of 4-nm-thick single crystalline zeolite nanosheets (ZNs) interlinked by Si–O–Si bonds between neighboring ZN surfaces. The dispersed open-pore ZNPs allowed formulating suspensions for tiling ZNP membranes on polymer substrates without requiring post-coating activation. A pinhole-free ZNP-tiled (ZNPT) membrane has been achieved on macroporous PVDF film by a self-repairing vacuum-assisted filtration coating method. The resultant ZNPT layer was ~500 nm-thick consisting of about 7 ZNP layers with inter-ZNP width and inter-ZNP entrance porosity around 9 nm and 2%, respectively. The ZNPT-PVDF membrane exhibited high selectivity to proton transport over vanadyl ion and low resistances to proton conduction in aqueous solutions. The membrane also demonstrated to function as an efficient ion separator for the vanadium redox flow battery. The reported synthesis of preactivated ZNP suspension may overcome the major hurdle to realizing polymer-supported ZN membranes, which is the inefficiency of existing methods in obtaining readily dispersible open-pore ZNs. The ZNPT-PVDF membrane can be a more affordable and sustainable alternative to the Nafion-based ion separation membranes.

1. Introduction

Zeolites with small and medium pore openings, such as the LTA and MFI types, can achieve perfect selectivity to water and proton permeation over hydrated metal ions by molecule and ion sieving effects [1–3]. Thus, zeolite membranes can be useful to high-efficiency proton-conduction in electrolyte solutions and desalination of concentrated brines for which traditional polymer membranes are inefficient [3–8]. The MFI-type zeolites are particularly desirable for such applications because their pore openings (~0.56 nm) are close to the maximum width (~0.60 nm) allowing total rejection of metal ions and hence can achieve low resistances to water and proton (mainly H_3O^+) transport with high selectivity [2,9]. However, the conventional zeolite membranes, which are polycrystalline films of intergrown isotropic crystals, require large thicknesses to minimize the nonselective intercrystalline spaces that lead to long diffusion pathways and large mass transport resistances [1,2,9].

The recent developments of zeolite nanosheets (ZNs) have enabled the developments of preferably oriented ultrathin zeolite membranes to simultaneously shorten the diffusion length and reduce intercrystalline spaces that improve both the mass transport rate and separation selectivity [10–14]. The existing ZN-based membranes are either multilayered-ZN films deposited from ZN suspensions or monolayer films of intergrown ZNs obtained via secondary growth of sparsely coated small-size ZN seeds [12,14–18]. The MFI-type ZN membranes, both pure-silica structure (silicalite) and aluminum-containing forms (ZSM-5), have been synthesized and demonstrated to provide extraordinary selectivity and permeation rates in separation of hydrocarbon isomers and pervaporation (PV) desalination of concentrated brines [15–17,19]. More recently, mixed matrix membranes with aligned discrete MFI ZNs embedded in ionic polymer films were demonstrated for efficient proton-selective ion conduction in redox flow batteries [20].

MFI ZNs with thicknesses of only one- or two unit-cell dimensions were obtained by exfoliation of layered zeolite precursors (LZP), which were synthesized using diquaternary or triquaternry ammonium structure directing agents (SDAs) [12,16,21]. These exfoliated single crystalline ZNs typically have small lateral sizes of 0.1–0.3 μm, which are inadequate for coating membranes without eliminating the nonselective or less selective inter-ZN spaces by secondary growth. Single crystal MFI ZNs were also directly synthesized by the nanoparticle-seeded secondary

* Corresponding author.
E-mail address: dongj@ucmail.uc.edu (J. Dong).

https://doi.org/10.1016/j.memsci.2022.121328
Received 29 October 2022; Received in revised form 22 December 2022; Accepted 25 December 2022
Available online 26 December 2022

growth method using diquaternary bis-1,5(tripropyl ammonium) pentamethylene diiodide (dC_5) as SDA [14]. However, each of the as-synthesized ZN crystals from this approach contains a seed-evolved high core, which must be removed for laminating multilayered ZN membranes with minimal inter-layer spaces. The removal of seed-cores is often done by fracturing and separation to obtain flat ZN fragments, which are much smaller in size than the core-containing crystals [16,17]. Furthermore, the ZNs require removal of SDA from the zeolitic channels that is achieved most effectively by calcination in air at >500 °C. However, the calcination process causes irreversible aggregation and deformation of ZNs, which make it difficult to formulate well-dispersed ZN suspensions necessary for coating pinhole-free ZN membranes. Also, the LZP exfoliation and seeded secondary growth methods both require complicated procedures that result in impractically low yields of dispersed ZNs after activation.

Although preparation of nonactivated ZN suspensions is relatively less challenging, the nonactivated ZN membranes require rigid ceramic substrates to allow high temperature calcination for SDA removal and protect the fragile ZN layers from bending and cracking. The development of more practical and economical polymer-supported ZN membranes has been so far very limited [15,22]. The chief challenge to synthesizing ZN membranes on polymers is the lack of efficient methods for preparing well-dispersed suspensions of preactivated ZNs necessary for coating thin membranes of desirable microstructures. Preactivated open-pore ZNs are required because post-coating activation of zeolitic pores is difficult on the polymer supports.

Herein, we report an efficient approach for synthesizing suspensions of preactivated ZN plates (ZNPs) of multilayered ZNs and subsequent fabrication of ZN membranes by directly tiling porous polyvinylidene fluoride (PVDF) films with the open-pore ZNPs. The ZNP-tiled (ZNPT) membranes on PVDF supports are studied for proton-selective ion conduction in aqueous solutions and demonstrated as ion separators for vanadium redox flow battery (RFB) operations.

2. Experimental section

2.1. Preparation of ZNP and its suspension

The preactivated silicalite ZNPs were prepared directly in liquid suspension to avoid irreversible aggregation that could occur during material processing in dry states. The suspension of well-dispersed preactivated ZNPs was achieved by a three-step procedure. These included the first step to grow flower-like assemblies of very large flat petals comprised of multiple layers of 4-nm thick single crystalline ZNs; the second step to harvest large-size flat ZNPs by mechanically disintegrating the ZN petals in liquid solvents after calcination activation; and the third step to make suspension of the dispersed preactivated ZNPs in solvents with compositions appropriate for directly tiling membranes on polymer substrates.

The flower-like very large ZN assemblies were synthesized by hydrothermal secondary growth of single crystal ZN seeds using our previously reported procedure [22]. For synthesis of the ZN seeds, single crystalline ZNs were first obtained by secondary growth of nanoparticle seeds in a precursor with molar composition of 80 tetraethyl orthosilicate (TEOS): 3.75 dC5: 20 KOH: 9500 H_2O [17]. The dC_5 SDA was homemade and the synthesis procedure was the same as those in the literature [14,17]. The resultant single crystals were retrieved after removing unreacted residuals by alternated washing with a 0.1 M KOH+1.0 M KCl solution (pH ~ 13) and deionized (DI) water, respectively. The single crystals were fractured by intensive sonication together with zirconia milling balls (4-mm-dia.) to dissociate flat ZN fragments from the seed-evolved cores. The sizes of these flat ZNs were further reduced by high energy ball milling to increase the ZN seed population for ZN assembly growth.

The ZN-seeded growth of ZN-assemblies were achieved by hydrothermal crystallization in a precursor solution containing 80 TEOS: 3.75 dC_5: 20 KOH: 12000 H_2O. The Si-based mass ratio of precursor to ZN seeds was 500–1000. The hydrothermal reaction was conducted in an autoclave at 140 °C for 4 days that was needed for fully maturing the ZN assemblies under this condition [23]. The solid products were collected by filtration after being stirred for 1 week in the 0.1 M KOH +1.0 M KCl solution to dissolve the unreacted amorphous silica residuals. The solid products were thoroughly rinsed with DI water and then dried for XRD and SEM characterizations to confirm the zeolite structure.

The solids with confirmed structures of ZN assemblies were calcined at 550 °C in air for 6 h to remove dC_5 SDA for zeolitic pore activation without collapsing the flower-like structure. The heating and cooling rates were 5 °C/min. The thermally activated very large ZN assemblies were sonicated in ethanol (EtOH) in a bed of 4-mm-dia zirconia milling balls to disintegrate the ZN flower petals into discrete flat ZNPs in the liquid medium. The initial suspension of ball-milled ZN assemblies was fractionated by sedimentation and centrifugation to retrieve uniform large-size ZNPs after removing the non-flat debris from the intersecting parts of the flower structure and most of the very small ZNP fragments. These nonuniform debris are undesirable for coating high quality membrane layers with minimized inter-ZNP spaces.

The slurry of preactivated ZNPs obtained above were directly dispersed in a controlled amount of a mixed solvent containing EtOH, dimethyl sulfoxide (DMSO, >99.9%, Fisher Chemical), and a small amount of dissolved PVDF. The dissolved PVDF was used as binder that can directly fuse the ZNP membrane layer with substrate surface of the same PVDF material. The PVDF is insoluble in water and EtOH. Thus, the PVDF binder was first dissolved in DMSO and then diluted by EtOH because DMSO and EtOH are miscible. The mass ratio of EtOH/DMSO mixed solvent was determined such that the concentration of DMSO was adequate to completely dissolve the PVDF binder but low enough to avoid dissolving and damaging the substrate surface during the membrane coating process. The suspension was dispersed by alternating sonication and stirring for ~2 h before use. The content of ZNPs was kept low enough to avoid settling under static condition for >5 min after stopping stirring.

2.2. Membrane fabrication

The polymer substrate used in this study was the commercially acquired porous PVDF film (# SF18140, hydrophilic surface, Tisch Scientific) with hydrophilic surface. The PVDF film had a thickness of 125 μm, an effective pore size of ~0.45 μm, and a porosity (ε_{PVDF}) of 83% according to the manufacturer specifications. The ε_{PVDF} was verified to be ~80% by weighing the film before and after soaking with EtOH and water. The PVDF film was confirmed to have excellent chemically and structurally stability in the highly oxidizing solution of 2 M $(VO_2)_2SO_4$ (V^{5+}) and 2 M H_2SO_4. After being immersed in the solution for 6 months, the PVDF sample only recorded a 2.0 ± 1.0% weight loss without noticeable change of pore structure (Fig. S1).

The ZNPs were tiled on the porous PVDF film over a 3.4 cm-diameter surface (i.e., effective coating area of 9.1 cm^2) by complete filtration of 3.5 mL ZNP suspension. The filtration-coating was accomplished under ambient pressure at upstream and a downstream vacuum pressure of ~0.1 bar using an apparatus shown in Fig. S2 (a). This vacuum forced filtration method has been proven effective for coating molecular and ionic sieve nanosheet-based membranes, including the fabrication of crosslinked-GO membrane on porous PTFE film as a high-performance RFB electrolyte membrane [24]. The PVDF substrate was presoaked with EtOH to avoid strong capillary suction when loading the suspension that could cause misaligned ZNP deposition in the beginning. It typically took 3 min to completely filter the liquid. The vacuum-forced filtration process has certain self-repairing effect as schematically illustrated by Fig. S2 (b). During the coating process, the solvent filtrate flow diminishes at the areas covered by ZNPs to slow down further ZNP deposition, and meanwhile, high filtrate flow continues at the uncovered spots that brings ZNPs to patch the defects.

The small amount of PVDF dissolved in the suspension was expected to mostly pass through the ZNP layer in the liquid filtrate with a small portion remaining to bind the ZNPs and fuse with the PVDF substrate surface. The resultant ZNP-tiled membrane on PVDF support (ZNPT-PVDF) was dried at 80 °C for 3 h under a vacuum pressure of <1.5 kPa, which was well below the DMSO saturation vapor pressure (~11 kPa at 80 °C) [25]. The dried membrane was subsequently cured at 120 °C for 3-h in a vacuum oven at ~24 kPa of absolute pressure. The above procedure was also used to fabricate the nonactivated ZNP-tiled membrane (NA-ZNPT-PVDF) for comparison. The nonactivated ZNPs were generated from the flower-like ZN assemblies after thorough cleaning but without calcination for SDA removal.

2.3. ZN material and membrane characterizations

2.3.1. Microstructure of ZNPT membrane

The microstructure of the single crystalline ZNs, multilayered ZNPs, and ZNPT-PVDF membranes were examined by scanning electron microscopy (SEM) and energy dispersive X-ray spectroscopy (EDS) using a FEI Scios DualBeam microscope equipped with Ametek Octane Super EDAX. The ZN materials were also characterized by transmission electron microscopy (TEM) and electron diffraction using a JEOL 2010F field emission electron microscope. The thicknesses of the ZNPs and the constituting single crystal ZNs were measured by a Veeco Dimension 3100 atomic force microscope (AFM) using height imaging and profiling under tapping mode. The crystal phase and orientation of the ZNPs and the tiled films were verified by X-ray diffraction (XRD) patterns measured by a PANalytical X'Pert Pro diffractometer with Cu Kα radiation ($\lambda = 1.5406$ Å). The XRD peak identification were based upon the standard spectrum of silicalite powders [26]. The micropore volumes, pore size distribution (PSD), and surface area of the ZN-assemblies were probed by N_2 adsorption-desorption measurements at 77 K using an Micromeritics ASAP 2020 unit [23]. The microporosimetry measurements were performed before and after calcination for SDA removal.

2.3.2. Ion transport and proton conduction

The ZNPT-PVDF membranes were experimentally studied for proton-selective ion transport and ion conduction in aqueous solutions, which are critical to applications as ion exchange membranes (IEMs). The tests used vanadium RFB electrolyte solutions as examples that is also of practical interest to electric energy storages. The ion diffusion measurements were conducted in a permeator with solutions circulated over a membrane area of 2.5 cm^2, which was described in our previous plications [3]. A RFB single cell shown in Fig. S3 was used for EIS, charge-discharge, and polarization curve measurements following the literature procedures [3,7]. The membrane working area was 1.2 × 1.2 (=1.44 cm^2) when mounted in the RFB cell. All the measurements were conducted at room temperature (~25 °C) and ambient pressure.

For ion diffusion measurements, a solution of 4/7 M $VOSO_4$ + 4/7 M H_2SO_4 was circulated in the feed side and a 1 M $MgSO_4$ solution was circulated in the permeate side for balancing ionic strength. The ion flux J_i (mol/cm^2·h) was obtained from the time-dependency of permeate ion concentration ($C_{p,i}$) in the linear region (i.e., the slope $dC_{p,i}/dt$) under constant feed concentrations,

$$J_i = \frac{V_p}{A_m} \bullet \frac{dC_{p,i}}{dt} \quad i = H^+, V^{4+}(VO^{2+}) \tag{1}$$

where the balancing solution volume in permeate side was $V_p = 20$ mL. The $\alpha_{H/V}$ is defined as the ratio of proton flux (J_{H^+}) to vanadyl ion flux ($J_{V^{4+}}$).

The area specific resistance (*ASR*) of the membrane was measured in 2 M H_2SO_4 solution by electrical impedance spectroscopy (EIS, Reference-600, Gamry Inc., USA). After the ion diffusion and *ASR* measurements, the ZNPT-PVDF membrane was tested as an ion separator for the vanadium RFB. The RFB charge-discharge and polarization curves were determined and compared with the commercial Nafion117® membrane, which is a widely used benchmark IEM for RFBs. The polarization curves were obtained within a short time to minimize change of the state of charge (SOC = $C_{V^{2+}}/(C_{V^{2+}} + C_{V^{3+}})$) during measurement, so that the total cell *ASR* (ASR_c) can be estimated based on the linear section of the polarization curve [3].

3. Results and discussion

3.1. ZN plates

The crystals grown from the silicalite nanoparticle seeds (Fig. 1a) were in typical rhombus shapes (Fig. 1b) with each containing a seed-evolved high core encircled by a uniform single layer nanosheet [14,17]. The flat ZN fragments were dissociated from the encircling sheets by sonication with zirconia milling balls and separated by centrifugation to remove the large debris from the center cores. These flat ZNs had unform thicknesses of ~4.5 nm (Fig. 1c and d) along the *b*-axis of MFI cell coordinate, namely in the direction of straight channels with nearly circular pore opening of 0.54 nm × 0.56 nm. These ZNs were further treated in the 0.1 M KOH +1.0 M KCl solution to ensure complete removal of amorphous silica residuals from the surface and expose the active sites for secondary growth.

The single crystalline ZN seeds were further downsized to ~0.2 × 0.2 μm^2 (Fig. 2a) by intensive sonication in liquid EtOH with the zirconia milling balls. The ZN assemblies grown from the small ZN seeds had flower-like structures comprised of very large petals of ZNPs (Fig. 2b). After SDA removal by calcination, the ZN assemblies remained in flower-like open structures without collapsing (Fig. S4a). Flat ZNPs with lateral dimensions around 2.0 μm × 2.0 μm (area ~4.0 μm^2, Fig. 2c) were obtained by sonication disintegration in EtOH and subsequent centrifugation fractionation processes. The separated large-size ZNPs were always kept in liquid solvent to avoid irreversible ZNP aggregation that would occur under drying conditions. These ZNPs consisted of multiple layers of single crystalline ZNs as can be seen in the SEM image of ball-milled pieces (Fig. 2d) where the ZN underlayers were unveiled by secondary electron emission. The ZNPs had thicknesses of 60 ± 10 nm according to the AFM examination (Fig. 2e) and the constituting single crystalline ZNs were ~ 4-nm-thick (Fig. 2f) [23]. The TEM and electron diffraction patterns showed that the stacked ZN layers and hence the entire ZNP were oriented with its thickness in the *b*-axis direction (Fig. 2e). The XRD tests further confirmed pure MFI crystal phase for the ZN assemblies and out-of-plane (020)-orientation (i.e., along *b*-axis) for the ZNP film tiled on glass (Fig. 2f).

The constituting single crystalline ZNs in the ZNPs are presumably bonded by condensation reaction ($\equiv Si-OH + HO-Si \equiv \rightarrow \equiv Si-O-Si \equiv +$ H_2 O) between adjacent ZN surfaces, which could occur during the hydrothermal crystallization and calcination processes. The multi-layered ZNPs had no evidence of delamination after sonication for two weeks in KOH (pH~13) and HCl (pH ~ 1.0) solutions, respectively. Exfoliation of ZNs from the calcined plates was not observed during intensive sonication after three cycles of freezing and thawing in toluene and water, respectively. However, a few isolated single crystal ZNs were found in sonicated suspensions in the 0.1 M KOH +1.0 M KCl solution after such freezing and thawing treatments of the nonactivated ZNPs (Fig. 2f). The results of BET tests for the ZN assemblies and conventional brick-shaped silicalite crystals (Fig. S4b and S4c) were consistent with our previous findings that indicated a small amount of micropores (~0.005 cm^3/g) in the ZNPs besides the zeolitic pore volume (0.165 ± 0.010 cm^3/g) [23]. These nonzeolitic micropores were micropore spaces between neighboring ZN surfaces with widths (d_{iz}) around ~1.4 nm, which were larger than the 0.56 nm zeolitic channels.

3.2. ZNPT membrane

The suspension used for coating membrane contained 0.02 wt%

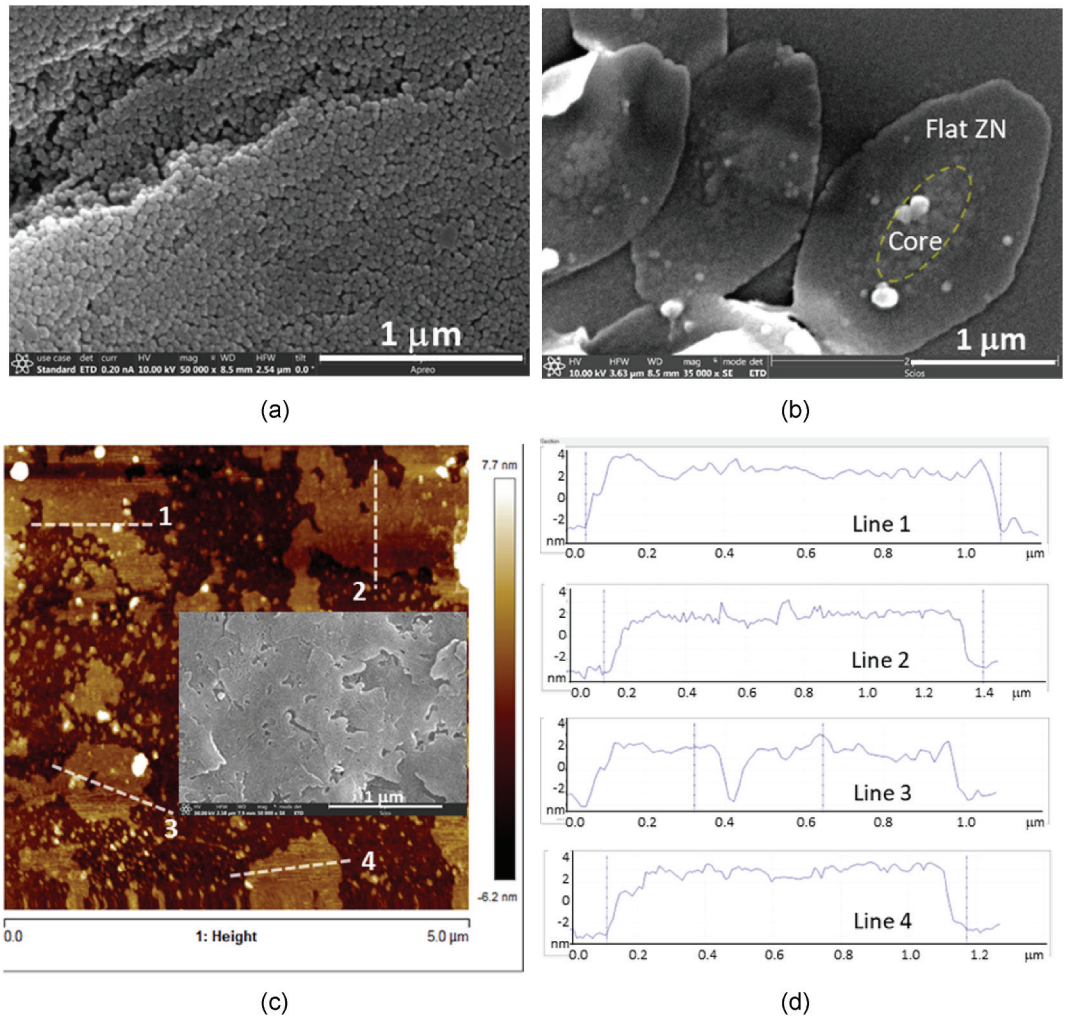

Fig. 1. The silicalite nanoparticle seeds and single layer ZNs generated by secondary growth: (a) SEM image of the seeds (diameters ~ 30 nm), (b) SEM picture of the as-synthesized rhombus crystals, (c) AFM height survey of the single crystalline flat ZNs (insert: SEM of ZNs after treatment in the KOH solution), and (d) height profiles of ZNs along lines indicated in (c).

ZNPs and 0.06 wt% dissolved PVDF. The mixed solvent had a EtOH/DMSO weight ratio of 2:1. This suspension composition was identified in synthesis of single crystalline ZN laminated membrane on the same PVDF film [22] and verified by additional experimental trials on the ZNPT membrane coating. Fig. 3 presents the SEM pictures of the bare PVDF substrate and the ZNPT-PVDF membrane. The pore size in the PVDF film shown by the SEM images (Fig. 3a and b) appeared to be d_p ~2 µm, which were larger than the manufacturer-stated average d_p of 0.90 µm. Pinhole-free ZNPT thin membranes (Fig. 3c and d) were obtained by single-time coating using the vacuum-assisted filtration method. The hilly membrane surface (Fig. 3d) shows that the tiled ZNPs conformed to the rough surface of the macroporous PVDF substrate.

The very large ZNPs were able to bridge over the surface pore openings and pinholes were effectively eliminated by the self-repairing effect of the vacuum-assisted filtration coating mechanism (Fig. S2b). The results of elemental survey over the ZNPT-PVDF cross-section (Fig. 3e and f) confirmed the existence of minimal PVDF binders in the ZNPT layer and absence of ZNP penetration into the PVDF substrate porosity. While the vacuum filtration method offers the advantage of improved membrane quality and reproducibility, it is inefficient for varying membrane thickness without altering the substrate and/or suspension properties. Uncovered spots or pinholes were often observed in thinner membranes formed from suspensions of much lower ZNP contents (e.g., membrane from 0.01 wt% ZNP shown in Fig. S5a and S5b); in the contrary, defects of misaligned ZNPs tended to form in thicker membranes from suspensions of much higher ZNP contents (e.g., membrane from 0.06 wt% ZNPs shown in Fig. S5c and S5d). The former had a drastically increased J_{H^+} but with diminished $\alpha_{H/V}$ while the latter caused significant decreases of both J_{H^+} and $\alpha_{H/V}$ (Table S1).

Based on the silicalite single crystal density ($\rho_z = 1.76$ g/cm^3) [27] and the 7.69×10^{-5} g/cm^2 ZNP deposited on the surface, a thickness of 437 nm (δ_{SCL}) could be expected if the ZNPT layer were a single crystal. Because the volume of inter-ZN spaces (d_{is} ~ 1.4 nm) was <3% of the total micropore volume of the ZNPs, the density of individual ZNP is almost same as a single crystal. Thus, it could be estimated that the ZNPT film was stacked by about 7 layers of ZNPs ($n_{ZNP} \sim \delta_{SCL}/t_{ZNP}$) for an average ZNP thickness (t_{ZNP}) of 60 nm. Consequently, the inter-ZNPT space widths (δ_{ip}, as depicted in Fig. 4a) in vertical direction were ~9 nm in the ~500-nm-thick (δ_{ZNPT}) dry ZNPT membrane as estimated by $\delta_{ip} = (\delta_{ZNPT} - \delta_{SCL})/n_{ZNP}$. These nanometer-scale inter-ZNP spaces were results of the microscopically uneven ZNP surfaces (Fig. 2d) and the insertion of the PVDF polymer binders between layered ZNPs. The minimal PVDF sparsely distributed between ZNPs (Fig. 3f) could narrow down the effective inter-ZNP spaces to improve the selectivity but meanwhile reduce the ion permeability and conductivity.

The ZNPT membrane layer had a bimodal pore system including intra-ZNP zeolitic pores (d_p ~ 0.56 nm) and inter-ZNP mesopores (δ_{ip} ~ 9 nm). The inter-ZN micropores (d_{is} ~ 1.4 nm) allow ion transfer

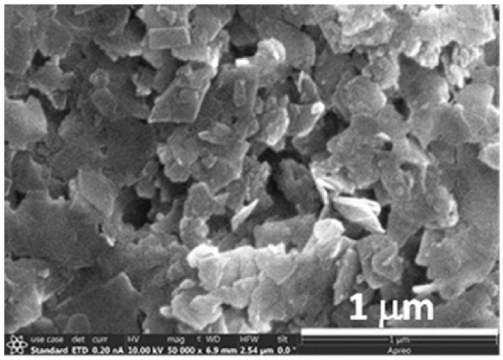

(a)

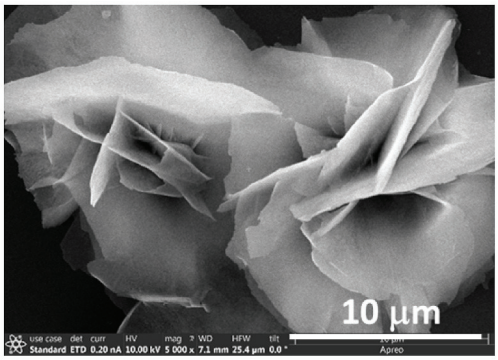

(b)

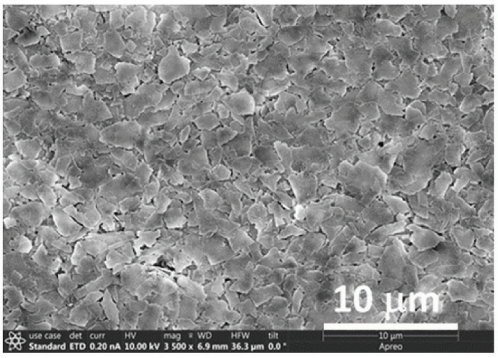

(c)

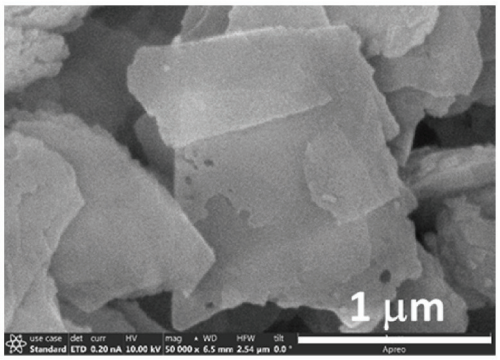

(d)

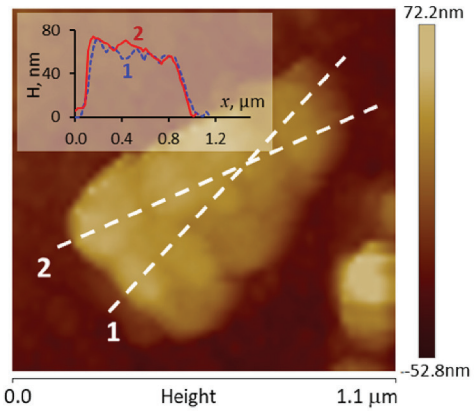

(e)

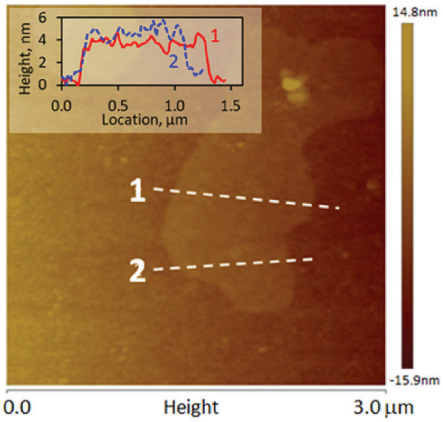

(f)

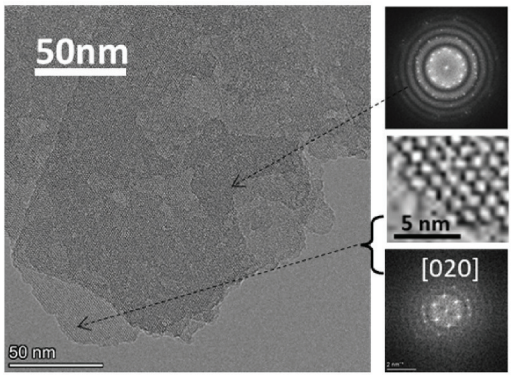

(g)

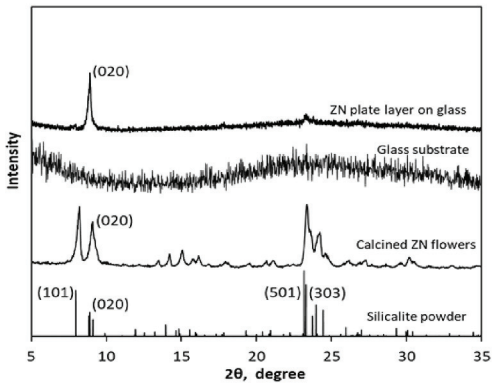

(h)

Fig. 2. Characterizations of ZN assemblies and dissociated ZNPs: (a) SEM image of the single crystalline ZN seeds, (b) SEM image of ZN assemblies, (c) SEM image of flat ZNPs disintegrated from the ZN assemblies, (d) SEM image of small ZNP debris revealing multilayered structure, (e) AFM height survey of a ZNP, (f) AFM height survey of a single crystalline ZN exfoliated from the ZNPs, (g) TEM image and electron diffraction patterns at multilayered layered (upper) and single-layered (lower) locations in ZNPs, and (h) XRD patterns of the ZN assemblies and ZNP film tiled on glass.

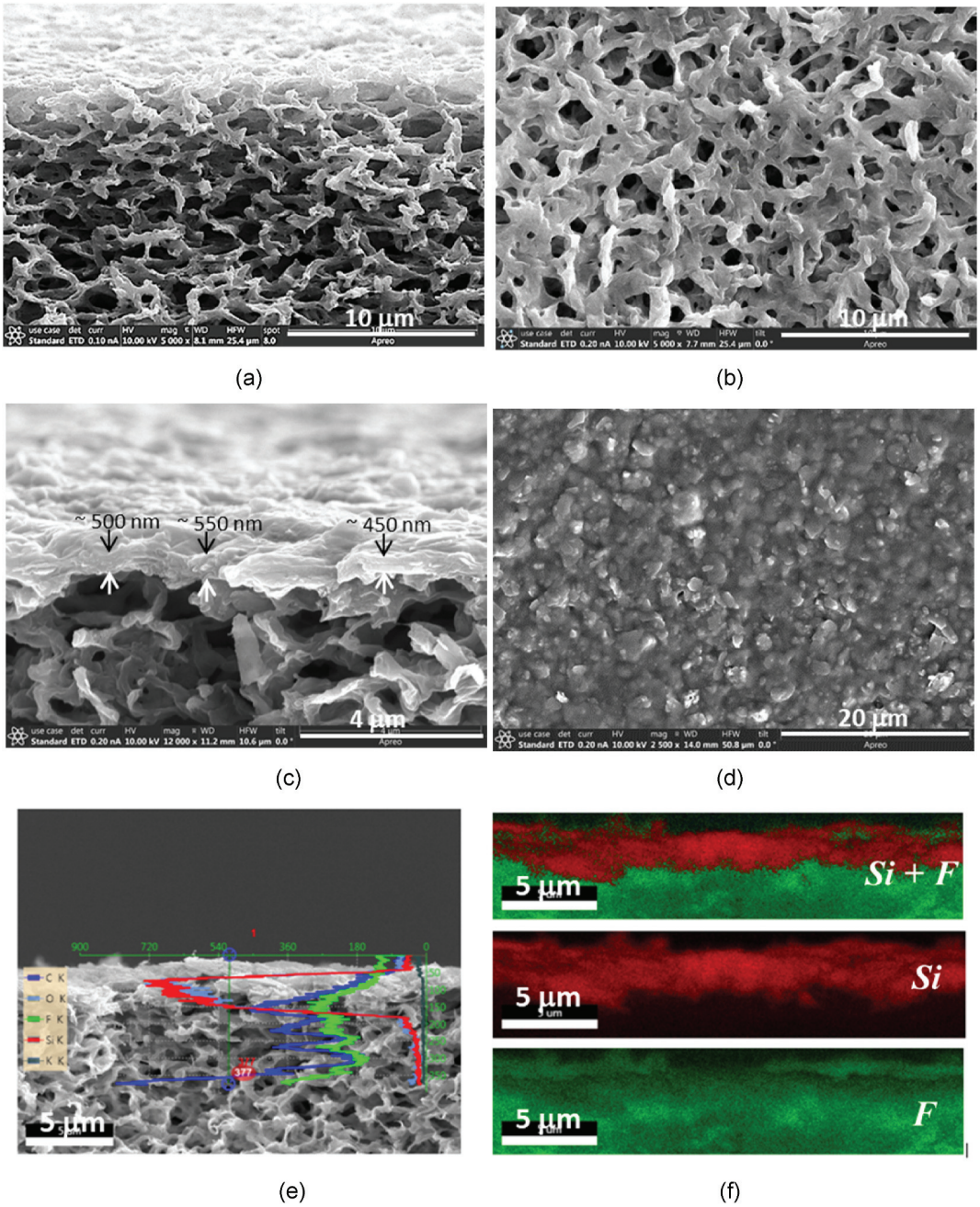

Fig. 3. Microscopic characterizations of the ZNPT-PVDF membrane: (a) cross-section of the substrate, (b) surface of the substrate, (c) cross-section of the ZNPT-PVDF membrane, (d) surface of the ZNPT layer, (e) EDS line scanning along the ZNPT-PVDF thickness, and (f) DES elemental imaging survey of the Si and F distribution over the ZNPT-PVDF cross-section.

through the multilayered ZNPs but are not expected to affect the selectivity because the zeolitic pores determine the accessibility to ions by ion sieving effects. Thus, in the ZNPT layer, protons transport through both intra-ZNP zeolitic pores and inter-ZNP spaces, but the metal ions could only diffuse through the inter-ZNP spaces (Fig. 4a). Apparently, it was the vertical inter-ZNP spaces (δ_{ip}) rather than the surface gaps between horizontally laid ZNPs (δ_{gs}) that determined the inter-ZNP transport rates because $\delta_{ip} \ll \delta_{gs}$ as depicted in Fig. 4a. The porosity of the inter-ZNP entrances (ε_{ip}) thus depends on the area (A_{ZNP}) and perimeter of individual ZNPs. The ε_{ip} could be estimated to be ~2.0% based on δ_{ip} ~9 nm and an average ZNP dimension L_{ZNP} of 2.0 µm (Fig. 3c):

$$\varepsilon_{ip} = \frac{N_{ZNP} \bullet A_{ip}}{N_{ZNP} \bullet A_{ZNP} + 0.25 N_{ZNP} \bullet A_{gp}} < \frac{4 \bullet \delta_{ip}}{L_{ZNP}} \quad (2)$$

where N_{ZNP}, A_{ZNP} ($=L_{ZNP}^2$), A_{ip} ($=4L_{ZNP} \bullet \delta_{ip}$), and A_{gp} ($= 4L_{ZNP} \bullet \delta_{gs}$) are the total number of ZNP covering membrane surface, the individual ZNP surface area, the inter-ZNP space area surrounding each ZNP, and the horizontal gap area surrounding each ZNP, respectively. Therefore, the J_i and $\alpha_{H/V}$ of ZNPT membrane depend on the sizes and morphological uniformity of the ZNPs. Fig. 4b and c are images of ZNP layers tiled on smooth glasses showing obviously smaller ε_{ip} in the film consisting of larger and more uniform ZNPs (Fig. 4b) than in the film of smaller and nonuniform ZNPs (Fig. 4c).

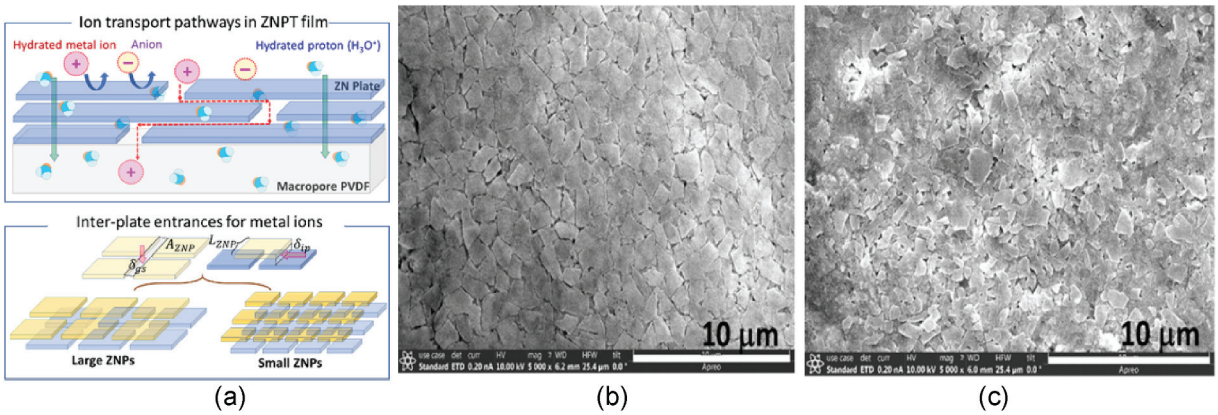

Fig. 4. Schematics showing ion transport pathways in the ZNPT-PVDF membrane: (a) bimodal pore system including zeolitic channels only accessible to proton and the inter-ZNP spaces allowing both proton and metal ion diffusion, (b) surface tiled by large and uniform ZNPs, and (c) surface tiled by nonuniform ZNPs (from residual after separating large ZNPs).

3.3. Ion transport rates and proton selectivity

Results of ion diffusion tests are presented in Fig. 5. For the bare PVDF substrate, both C_{p,H^+} and $C_{p,V^{4+}}$ increased rapidly after a relatively slow increase in the first ~0.3 h (Fig. 5a). The brief transition in the beginning was caused by fast stabilization of concentration gradients across the macroporous film. The J_{H^+} and $J_{V^{4+}}$ through the bare substrate were 8.10×10^{-3} mol/cm^2·h and 4.50×10^{-3} mol/cm^2·h, respectively, that gave an $\alpha_{H/V}$ of 1.8. Thus, the substrate was nonselective for the permeating ions as the selectivity would near unity (~0.9) when normalized by driving forces, i.e., concentration differences between the two sides (Table S2).

The membrane tiled by nonactivated ZNPs (NA-ZNPT-PVDF) had thickness and surface morphology that were about the same as those of the ZNPT-PVDF (Fig. S6). It exhibited J_{H^+} and $J_{V^{4+}}$ of 3.35×10^{-6} mol/cm^2 h and 7.40×10^{-7} mol/cm^2 h, respectively, which were only 0.041% and 0.016% of those on the bare substrate because of the impermeability of the nonactivated ZNPs. The J_{H^+} experienced a ~4 h transition period before stabilization (Fig. 5a). The slow stabilization of flux was likely caused by two factors: the first was the ZNP surface protonation in the highly acidic solution that could develop ZNP surface charges and slightly increase the δ_{ip}; and the second was the slow ion

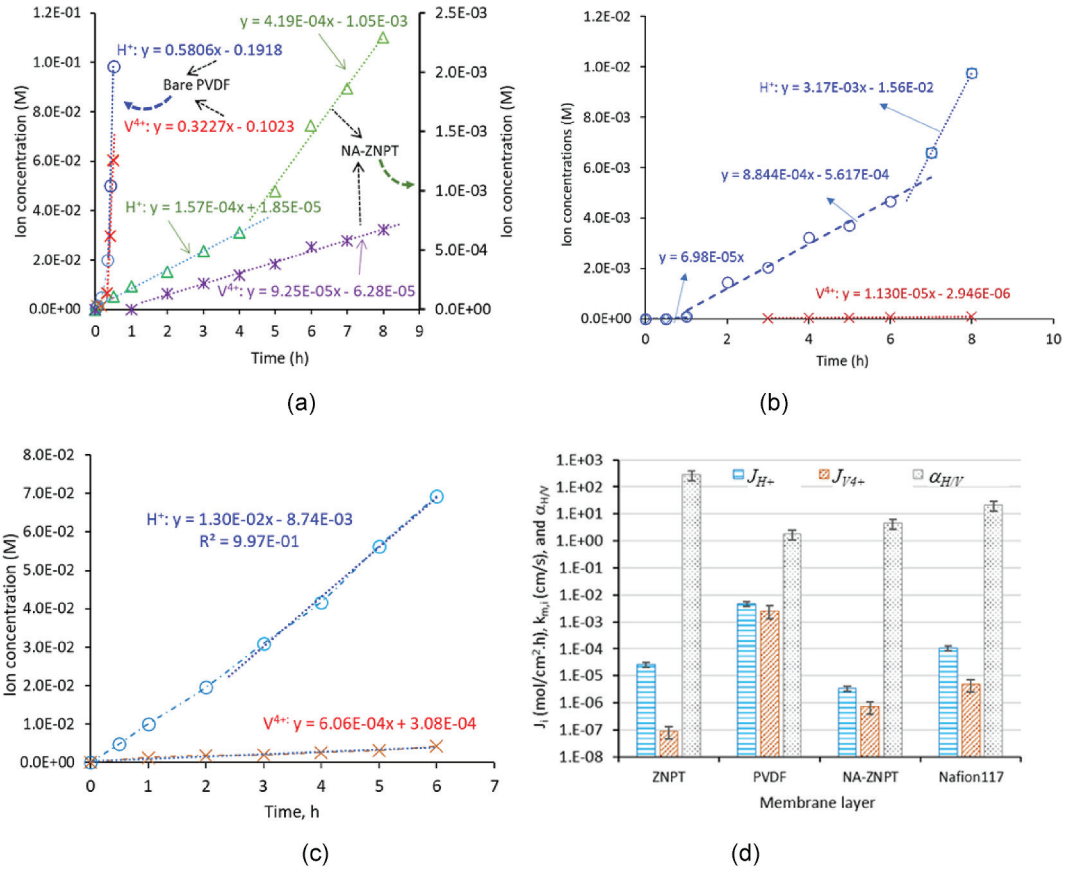

Fig. 5. Measurements of ion diffusion through membranes: (a) $C_{p,i}$ *vs.* t for bare PVDF and the NA-ZNPT-PVDF, (b) $C_{p,i}$ *vs.* t for ZNPT-PVDF, (c) $C_{p,i}$ *vs.* t for Nafion117®, and (d) J_i and $\alpha_{H/V}$ for different membrane layers.

diffusion through the long-length zigzagged nanometer-scale inter-ZNP spaces. The NA-ZNPT showed a small $\alpha_{H/V}$ of ~4.5 because of the nanometer-scale inter-ZNP space sizes (δ_{ip} ~9 nm).

The C_{p,H^+} exhibited three distinct regions of time dependency for the ZNPT-PVDF membrane with increasing slopes (Fig. 5b). The membrane has low J_{H^+} of 5.58×10^{-7} mol/cm^2·h on average in the first hour that could be attributed to permeation through the inter-ZNP spaces. The Intermediate region was likely resulted from inter-ZNP space evolution by surface protonation/solvation, ion sorption in inter-ZN micropores (d_{is} ~ 1.4 nm) in ZNPs, and development of permeation through mixed paths of intra-ZNP and inter-ZNP porosities. A J_{H^+} of 7.08×10^{-6} mol/cm^2·h was estimated for the middle stage. The J_{H^+} reached 2.54×10^{-5} mol/cm^2·h in about 6 h. The vanadyl ions only could diffuse through the inter-ZNP spaces, which had a very small porosity (ε_{ip} ~2.0%). The $C_{p,V^{4+}}$ was too low to be accurately quantified by the UV spectroscopic method (detection limit ~2.4×10^{-5} M; Fig. S7) in the first 3 h and showed a very small but nearly constant increasing rate afterwards. A $J_{V^{4+}}$ of 9.04×10^{-8} mol/cm^2·h was estimated based on the data after 4 h that led to an $\alpha_{H/V}$ of ~280.

Because the transport resistance of the nonselective macropore PVDF substrate was much smaller than that of the ZNPT layer, as indicated by its very high ion fluxes, switching the ZNPT surface orientation from facing the feed to facing permeate side had rather insignificant effect on the ion selectivity and fluxes (Fig. S8). However, during the transition period, notably lower J_{H^+} was observed for ZNPT surface facing the permeate side as compared to facing the feed (Fig. S8). In the literature [28], similar effects of asymmetric membrane positioning on the ion transport behavior were reported and explained by the variations of concentration gradients across the active layer based on the serial resistor transport model. For the ZNPT-PVDF, the slower J_{H^+} increase in transition period when the water-soaked substrate faced the feed was likely also in part caused by delayed contact and equilibration of feed solution with the ZNPT layer.

The surfaces of ZNPs were chemically different before and after calcination. The nonactivated ZNP contained dC_5 at the zeolitic pore mouths of external surface and at inter-ZN spaces within the ZNP while the activated ZNPs were free of organics. These could cause different ZN surface ionization/solvation and inter-ZNP space evolution behaviors in the electrolytes between the activated and nonactivated ZNPs. The organic-free silica surfaces are expected to be more readily protonated to form higher surface ionicity than the organic-containing surfaces. Consequently, the proton and vanadyl ion diffusion rates through the inter-ZNP and inter-ZN (intra-ZNP) spaces could vary in the NA-ZNPT and ZNPT layers. The ZNPT-PVDF exhibited dramatically higher J_{H^+} that was caused by diffusion through the zeolitic pores. Meanwhile, it showed a substantially reduced $J_{V^{4+}}$ as compared to the NA-ZNPT. The smaller $J_{V^{4+}}$ of ZNPT membrane could be attributed to the greater surface protonation in the ZNPT, which created larger resistances to VO^{2+} diffusion through the nanometer-scale inter-ZNP spaces (δ_{ip} ~ 9 nm).

Unlike the ZNPT-PVDF, the Nafion117® membrane had no appreciable ramp of proton permeation rate (Fig. 5c) because the fully hydrated sulfonated tetrafluoroethylene surface releases proton instantly upon contacting the pH-neutral solution. A ZNPT-PVDF membrane was also presoaked with 2 M H_2SO_4 solution and then tested for ion diffusion (Fig. S9). Like the acidic Nafion membrane, the H_2SO_4-soaked membrane caused a much earlier onset of C_{p,H^+} increase in the permeate than did the water-soaked membrane because the former could also instantly release H^+ to sweep solution. Meanwhile, a delayed permeation of VO^{2+} still occurred to the H_2SO_4-soaked membrane because of the time needed for solution displacement before VO^{2+} penetrated through the membrane layers.

Because of its high concentration of solvated proton in the nanometer-scale water channels (d_p ~ 2.5 nm [3,29]), the Nafion117 had a J_{H^+} (1.04×10^{-4} mol/cm^2·h), which was 4 times that of the ZNPT-PVDF. However, the relatively large-size water channels also allowed a $J_{V^{4+}}$ of 4.85×10^{-6} mol/cm^2·h that was 54 times that of the ZNPT-PVDF. The Nafion117 had an $\alpha_{H/V}$ of ~21.5, which was much lower than that of the ZNPT-PVDF ($\alpha_{H/V}$ ~ 280). The ZNPT membrane was able to effectively restrict metal ion transport mainly because of its very small ε_{ip} (~2.0%). The J_{H^+}, $J_{V^{4+}}$ and $\alpha_{H/V}$ of different membranes obtained from the diffusion data in Fig. 5a-c are represented in Fig. 5d and tabulated in Table S2.

3.4. Proton conduction

Results of the EIS measurements are presented in Fig. 6a. The *ASR* of the individual membrane layers (ASR_m; m = PVDF, ZNPT, NA-ZNPT, and Nafion117) were in the order of ASR_{PVDF} ($0.029\ \Omega \bullet cm^2$) « $ASR_{Nafion117}$ ($0.36\ \Omega \bullet cm^2$) < ASR_{ZNPT} ($0.45\ \Omega \bullet cm^2$) « $ASR_{NA-ZNPT}$ ($4.15\ \Omega \bullet cm^2$) (Fig. 6b). The ion conductivity of each layer (σ_m) estimated based on its thickness δ_m and ASR_m, i.e., $\sigma_m = \delta_m/ASR_m$, were σ_{PVDF} ~ $4.34 \times 10^{-1}\ \Omega^{-1} \bullet cm^{-1}$, $\sigma_{NA-ZNPT}$ ~ $1.21 \times 10^{-5}\ \Omega^{-1} \bullet cm^{-1}$, σ_{ZNPT} ~ $1.12 \times 10^{-4}\ \Omega^{-1} \bullet cm^{-1}$, and σ_{Nafion} ~ $5.08 \times 10^{-2}\ \Omega^{-1} \bullet cm^{-1}$. The difference of σ_m between the ZNPT and NA-ZNPT layers generally agrees with the difference of their J_{H^+} (Fig. 5d), i.e., $\sigma_{ZNPT}/\sigma_{NA-ZNPT} \approx 9.3$ and $J_{H^+}(ZNPT)/J_{H^+}(NA-ZNPT) \approx 7.6$. This suggests that the ion tarnsport rates through the inter-ZNP spaces in the ZNPT membrane may be reasonably represented by the values of the NA-ZNPT layer. The σ_m is determined by the proton permeability of the membrane material, i.e., $P_{b,H^+} = C_{H^+}D_{H^+}$, where C_{H^+} and D_{H^+} are H^+ concentration and diffusivity in the membrane material, respectively [3]. Thus, the highly ionic Nafion117 has much greater σ_m than the intrinsically nonionic ZNPT [3,30]. Although $\sigma_{Nafion117}$ was ~450 times the σ_{ZNPT}, the ASR_{ZNPT} was only 1.25 times the $ASR_{Nafion117}$ because the δ_{ZNPT} was far smaller than the $\delta_{Nafion117}$.

3.5. Operation in RFB

The ZNPT-PVDF membrane was tested to function as an ion separator for the vanadium RFB equipped with carbon felt electrodes. The charge-discharge curves at constant current densities (i) and discharge polarization curves were measured using 10 mL catholyte solution containing 2 M $(VO_2)_2SO_4$ (V^{5+})+2 M (H_2SO_4) and 10 mL anolyte solution with 2 M VSO_4 (V^{2+})+2 M (H_2SO_4) [3]. The membrane *ASR* was reexamined by EIS measurements under the RFB operation conditions.

Fig. 7a presents the charge-discharge curves for the vanadium RFB equipped with ZNPT-PVDF and Nafion117 membrane, respectively. The RFB performed slightly better with the ZNPT-PVDF than with the Nafion117 membrane in terms of Coulombic efficiency (CE = [discharge time]/[charging time]), voltage efficiency (VE = [discharging voltage]/[charging voltage]), and energy efficiency (EE = CE × VE) (Fig. 7b). At a low i = 30 mA/cm^2, the RFB with ZNPT-PVDF obtained slightly higher CE (~87%) than that with the Nafion117 (CE ~ 84%). The better CE on the ZNPT-PVDF was caused by its high $\alpha_{H/V}$ that reduced metal ion crossover, especially over long operation times needed for low current densities. The CE was drastically enhanced for both membranes at a higher current density of 90 mA/cm^2 where the ZNPT-PVDF achived CE of ~99% and EE of 82% and the Nafion117 obtained CE ~99% and EE ~81%.

Fig. 7c presents polarization curves for the RFB when equipped with the ZNPT-PVDF and Nafion117 membrane, respectively, with the corresponding power density ($P_e = i \bullet V$, mW/cm^2). The linear sections of the curves (Fig. S10) were used to estimate the whole RFB cell and membrane *ASR* [3,31]. The *ASR* of the ZNPT-PVDF was estimated from the polarization curve by excluding the resistances of other cell components (mainly including carbon electrodes and graphite current collectors). The thus-estimated *ASR* of the ZNPT-PVDF was ~$0.71\ \Omega \bullet cm^2$, which was 50% higher than the value measured by EIS in the 2 M H_2SO_4 solution (*ASR* ~$0.48\ \Omega \bullet cm^2$). In contrast, the *ASR* of Nafion117 derived

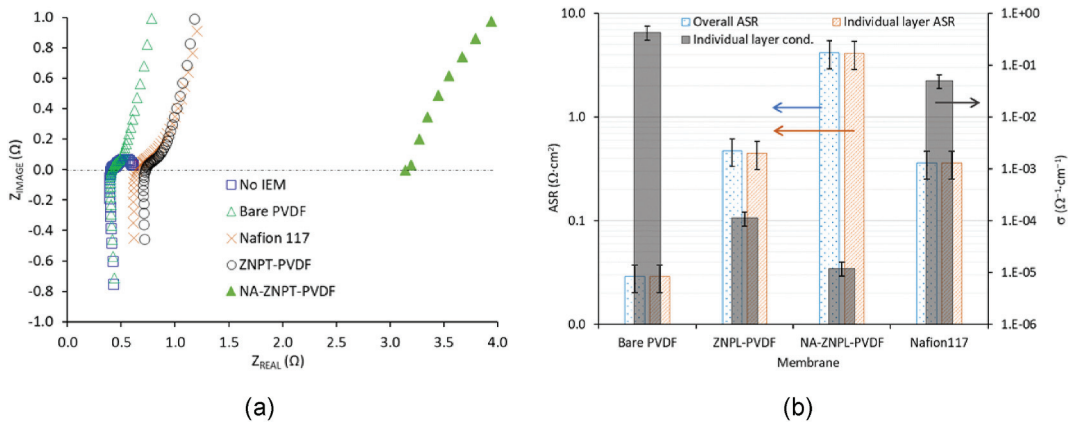

Fig. 6. Results of IES tests for membranes in 2 M H_2SO_4: (a) EIS spectra and (b) overall ASR of multileyerd membranes, and ASR_m and σ_m of the individual membrane layers.

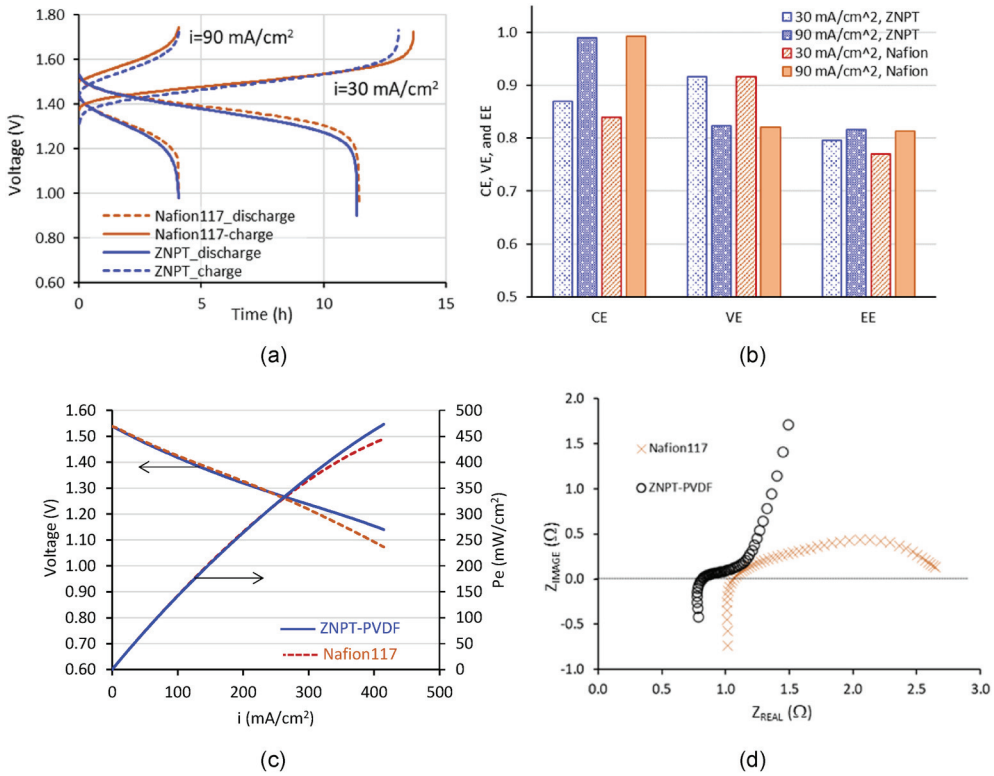

Fig. 7. Performances of ZNPT-PVDF and Nafion117 membranes as ion separators for Vanadium RFB: (a) charge-discharge curves at current densities of 30 and 90 mA/cm^2, respectively, (b) CE, VE, and EE from charge-discharge data in (a), (c) polarization curves and corresponding power density (P_e) dependencies on current density, (d) EIS spectra of the RFB in charged electrolyte solutions.

from the polarization curve was ~0.86 $\Omega \bullet cm^2$, which was 140% higher than that measured by EIS in the 2 M H_2SO_4 solution (ASR ~0.36 $\Omega \bullet cm^2$). For confirmation, EIS measurements were also taken for the RFB after charging (Fig. 7d). The EIS measurements under RFB operation conditions also showed a smaller ASR for the ZNPT-PVDF (~0.60 $\Omega \bullet cm^2$) than for Nafion117 (ASR ~0.95 $\Omega \bullet cm^2$).

The substantial increase of ASR for Nafion117 in RFB operation conditions has been found to be primarily caused by the penetration of vanadium ions. The penetration and retention of vanadium ions contaminate the nanoscale water channels (d_p ~2.5 nm) that increases rsistance to proton condution in Nafion [32–34]. Although vanadium ions can also enter the ZNPT layer through the very small amount of 9-nm-width inter-ZNP spaces (ε_{ip} ~ 2.0%), proton conduction in the membrane is much less affected because the zeolitc channels as the main pathways for proton transport are inaccessible to metal ions. Improved VE and P_e are hence expected from the ZNPT-PVDF over the Nafion117 because the former offers smaller ASR in RFB operation conditions to reduce internal Ohmic losses ($= i \bullet ASR$), especially at relatively high current densities.

The ZNPT-PVDF membrane-equipped RFB was also tested by 10 cycles of charge-discharge operation over ~50 h. The experiments were performed at a current density of 60 mA/cm^2 with 1 M V^{2+}/V^{3+} + 2 M H_2SO_4 anolyte and 1 M VO_2^+/VO^{2+} (V^{5+}/V^{4+}) + 2 M H_2SO_4 catholyte. As shown in Fig. 8a, the ZNPT-PVDF maintained stable energy efficiency around 79% over the 10 cycles. The polarization curves were measured after the cyclic operation for three different electrolyte concentrations. The results in Fig. 8b indicated similarly good performances that were

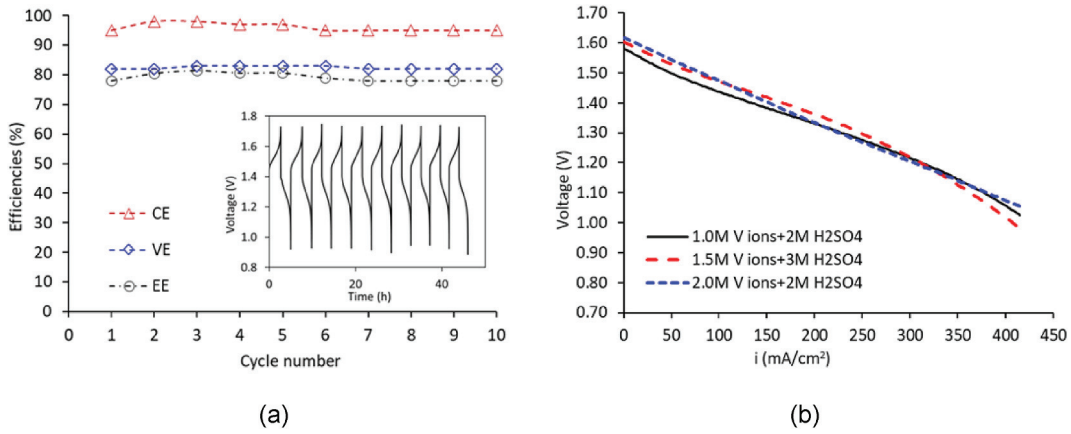

Fig. 8. Cyclic operation and polarization curves for the RFB equipped with the ZNPT-PVDF membrane: (a) CE, VE, and EE for the 10-cycle operation (insert: charge-discharge curves), and (b) polarization curves for electrolyte solutions with vanadium ion concentrations of 1.0 M, 1.5 M, and 2.0 M, respectively.

comparable to that in Fig. 7c. The membrane remained in the RFB operation environments for ~4 weeks during these measurements including times for initial generation of the anolytes and catholytes from $VOSO_4$ precursor solutions. The SEM examinations after RFB operations showed no obvious changes in membrane structure and integrity based on survey over large areas (Fig. S11).

4. Conclusion

Preactivated silicalite ZNPs of large lateral dimensions (~2.0 × 2.0 μm^2) and nanometer thicknesses (~60 nm) were obtained in liquid-dispersed state by mechanically disintegrating flower-like assemblies of vary large multilayered ZN petals. The dispersed open-pore ZNPs allowed the preparation of well-dispersed ZNP suspensions that overcame the major hurdle to synthesizing polymer-supported ZN membranes, which is the current inefficiency in obtaining dispersible open-pore ZNs. Ultrathin preactivated ZNP membranes were tiled on porous PVDF films by a vacuum-assisted total filtration method. Because of the self-repairing effects of the forced filtration-deposition mechanism, pinhole-free ZNP-tiled membranes (ZNPT-PVDF) were achieved by a single time coating. The resultant ZNPT layer had a thickness of ~500 nm, which consisted of about 7 ZNP layers with vertical inter-ZNP space and porosity about 9 nm and 2%, respectively. The ZNPT-PVDF membrane exhibited high selectivity to proton transport over vanadyl ions and low resistance to proton conduction in aqueous solutions. The membrane also demonstrated effectiveness as an ion separator for the vanadium RFB, although the performance stability over longer terms is yet to be performed. The ZNPT-PVDF membrane can be a more affordable and sustainable alternative to Nafion-based ion separation membranes.

Declaration of competing interest

The authors declare that they have no known competing financial interests or personal relationships that could have appeared to influence the work reported in this paper.

Data availability

Data will be made available on request.

Acknowledgements

This research was supported by the U.S. National Science Foundation (Grant # CBET-1935205) and the U.S. Department of Energy Office of Science (Grant # DE-SC0020011).

Appendix A. Supplementary data

Supplementary data to this article can be found online at https://doi.org/10.1016/j.memsci.2022.121328.

References

[1] J. Lin, S. Murad, A computer simulation study of the separation of aqueous solution using thin zeolite membranes, Mol. Phys. 99 (14) (2001) 1175–1181.
[2] S.H. Jamali, T.J.H. Vlugt, L.C. Lin, Atomistic understanding of zeolite nanosheets for water desalination, J. Phys. Chem. C 121 (2017) 11273–11280.
[3] Z. Xu, I. Michos, Z. Cao, W. Jing, X. Gu, K.R. Kinkel, S. Murad, J. Dong, Proton-selective ion transport in ZSM-5 zeolite membrane, J. Phys. Chem. C 120 (46) (2016) 26386–26392.
[4] L. Li, J. Dong, T.M. Nenoff, R. Lee, Desalination by reverse osmosis using MFI zeolite membranes, J. Membr. Sci. 243 (2004) 401–404.
[5] M.C. Duke, J. O'Brien-Abraham, N. Milne, B. Zhu, J.Y.S. Lin, J.C. Diniz da Costa, Seawater desalination performance of MFI type membranes made by secondary growth, Separ. Purif. Technol. 68 (2009) 343–350.
[6] M. Drobek, C. Yacou, J. Motuzas, A. Julbe, L. Ding, J.C.D. da Costa, Long term pervaporation desalination of tubular MFI zeolite membranes, J. Membr. Sci. 415 (2012) 816–823.
[7] Z. Xu, I. Michos, X. Wang, R. Yang, X. Gu, J. Dong, Zeolite ion exchange membrane for redox flow battery, Chem. Commun. 50 (2014) 2416–2419.
[8] J. Dong, Z. Xu, S. Yang, S. Murad, K.R. Kinkel, Zeolite membranes for ion separations from aqueous solutions, Curr. Opin. Chem. Eng. 8 (2015) 15–20.
[9] S. Murad, K. Oder, J. Lin, Molecular simulation of osmosis, reverse osmosis, and electro-osmosis in aqueous and methanolic electrolyte solutions, Mol. Phys. 95 (1998) 401–408.
[10] A. Corma, V. Fornes, S.B. Pergher, Th L.M. Maesen, J.G. Buglass, Delaminated zeolite precursors as selective acidic catalysts, Nature 396 (1998) 353–356.
[11] D. Kerstens, B. Smeyers, J. Van Waeyenberg, Q. Zhang, J. Yu, B.F. Sels, State of the art and perspectives of hierarchical zeolites: practical overview of synthesis methods and use in catalysis, Adv. Mater. 32 (2020), 2004690.
[12] K. Varoon, X. Zhang, B. Elyassi, D.D. Brewer, M. Gettel, S. Kumar, J.A. Lee, S. Maheshwari, A. Mittal, C.-Y. Sung, M. Cococcioni, L.F. Francis, A.V. McCormick, K.A. Mkhoyan, M. Tsapatsis, Dispersible exfoliated zeolite nanosheets and their application as a selective membrane, Science 334 (2011) 72–75.
[13] M. Choi, K. Na, J. Kim, Y. Sakamoto, O. Terasaki, R. Ryoo, Stable single-unit-cell nanosheets of zeolite MFI as active and long-lived catalysts, Nature 461 (2009) 246–249.
[14] M.Y. Jeon, D. Kim, P. Kumar, P.S. Lee, N. Rangnekar, P. Bai, M. Shete, B. Elyassi, H. S. Lee, K. Narasimharao, S.N. Basahel, S. Al-Thabaiti, W. Xu, H.J. Cho, E.O. Fetisov, R. Thyagarajan, R.F. DeJaco, W. Fan, K.A. Mkhoyan, J.I. Siepmann, M. Tsapatsis, Ultra-selective high-flux membranes from directly synthesized zeolite nanosheets, Nature 543 (2017) 690–694.
[15] H. Zhang, Q. Xiao, X. Guo, N. Li, P. Kumar, N. Rangnekar, M.Y. Jeon, S. Al-Thabaiti, K. Narasimharao, S.N. Basahel, B. Topuz, F.J. Onorato, C.W. Macosko, K. A. Mkhoyan, M. Tsapatsis, Open-pore two-dimensional MFI zeolite nanosheets for the fabrication of hydrocarbon-isomer-selective membranes on porous polymer supports, Angew. Chem. Int. Ed. 55 (2016) 7184–7187.
[16] D. Kim, Y. Jeon, B.L. Stottrup, M. Tsapatsis, Para-xylene ultra-selective zeolite MFI membranes fabricated from nanosheet monolayers at the air-water interface, Angew. Chem. Int. Ed. 57 (2018) 489–494.
[17] Z. Cao, S. Zeng, Z. Xu, A. Arvanitis, S. Yang, X. Gu, J. Dong, Ultrathin ZSM-5 zeolite nanosheet laminated membrane for high-flux desalination of concentrated brines, Sci. Adv. 4 (2018) eaau8634.
[18] D. Kim, S. Ghosh, N. Akter, A. Kraetz, X. Duan, G. Gwak, N. Rangnekar, J. R. Johnson, K. Narasimharao, M.A. Malik, S. Al-Thabaiti, B. McCool, J.

A. Boscoboinik, K.A. Mkhoyan, M. Tsapatsis, Twin-free, directly synthesized MFI nanosheets with improved thickness uniformity and their use in membrane fabrication, Sci. Adv. 8 (2022), eabm8162.
[19] B. Min, S. Yang, A. Korde, Y.H. Kwon, C.W. Jones, S. Nair, Continuous zeolite MFI membranes fabricated from 2D MFI nanosheets on ceramic hollow fibers, Angew. Chem. Int. Ed. 58 (2019) 8201–8205.
[20] Y. Xia, H. Cao, F. Xu, Y. Chen, Y. Xia, D. Zhang, L. Dai, K. Qu, C. Lian, K. Huang, W. Xing, W. Jin, Z. Xu, Polymeric membranes with aligned zeolite nanosheets for sustainable energy storage, Nat. Sustain. 5 (2022) 1080–1091.
[21] L. Meng, B. Mezari, M.G. Goesten, E.J.M. Hensen, One-step synthesis of hierarchical ZSM-5 using cetyltrimethylammonium as mesoporogen and structure-directing agent, Chem. Mater. 29 (2017) 4091–4096.
[22] Z. Cao, L. Iskhakova, X. Sun, Z. Tang, J. Dong, ZSM-5 zeolite nanosheet-based membranes on porous polyvinylidene fluoride for high-flux desalination, ACS Appl. Nano Mater. 4 (3) (2021) 2895–2902.
[23] Z. Cao, L. Iskhakova, X. Sun, N.D. Anjikar, S. Yang, J. Dong, Self-seeded growth of very large open-structured zeolite nanosheet assemblies with extraordinary micropore accessibility, Microporous Mesoporous Mater. 336 (2022), 111854.
[24] S. Kim, J. Choi, C. Choi, J. Heo, D.W. Kim, J.Y. Lee, Y.T. Hong, H.-T. Jung, H.-T. Kim, Pore-size-tuned graphene oxide frameworks as ion-selective and protective layers on hydrocarbon membranes for vanadium redox-flow batteries, Nano Lett. 18 (6) (2018) 3962–3968.
[25] G. Jakli, W.A. van Hook, The vapor pressures of dimethyl sulfoxide and hexadeuterodimethyl sulfoxide from about 313 to 453 K, J. Chem. Thermodyn. 4 (6) (1972) 857–864.
[26] C. Baerlocher, L.B. McCusker, D.H. Olson, Atlas of zeolite framework types, in: Structure Commission of the International Zeolite Association, seventh ed., Elsevier, Oxford, UK, 2007.
[27] E.M. Flanigen, J.M. Bennett, R.W. Grose, J.P. Cohen, R.L. Patton, R.M. Kirchner, J. V. Smith, Silicalite, a new hydrophobic crystalline silica molecular sieve, Nature 271 (5645) (1978) 512–516.
[28] W. Lee, M. Jung, D. Serhiichuk, C. Noh, G. Gupta, C. Harms, Y. Kwon, D. Henkensmeier, Layered composite membranes based on porous PVDF coated with a thin, dense PBI layer for vanadium redox flow batteries, J. Membr. Sci. 591 (2019), 117333.
[29] K. Schmidt-Rohr, Q. Chen, Parallel cylindrical water nanochannels in nafion fuel-cell membranes, Nat. Mater. 7 (2008) 75–83.
[30] R. Yang, Z. Xu, S. Yang, L. Li, A. Angelopoulos, J. Dong, Nonionic zeolite membrane as potential ion separator in redox-flow battery, J. Membr. Sci. 450 (2014) 12–17.
[31] D. Aaron, Z. Tang, A.B. Papandrew, T.A. Zawodzinski, Polarization curve analysis of all-vanadium redox flow batteries, J. Appl. Electrochem. 41 (2011) 1175–1182.
[32] M. Vijayakumar, M.S. Bhuvaneswari, P. Nachimuthu, B. Schwenzer, S. Kim, Z. G. Yang, J. Liu, G.L. Graff, S. Thevuthasan, J.Z. Hu, Spectroscopic investigations of the fouling process on nafion membranes in vanadium redox flow batteries, J. Membr. Sci. 366 (2011) 325–334.
[33] B. Schwenzer, J. Zhang, S. Kim, L. Li, J. Liu, Z. Yang, Membrane development for vanadium redox flow batteries, ChemSusChem 4 (2011) 1388–1406.
[34] I. Michos, Z. Cao, Z. Xu, W. Jing, J. Dong, Investigations on mesoporous glass membrane as ion separator for redox flow battery, Batteries 5 (6) (2019) 1–24.

Preactivated Zeolite Nanosheet Plate-Tiled Membrane on Porous PVDF Film: Synthesis and Study of Proton-Selective Ion Conduction

Landysh Iskhakova, Zishu Cao, Xinhui Sun, Jan Gabski, Junhang Dong *
Department of Chemical and Environmental Engineering, University of Cincinnati, Cincinnati, OH 45221, USA.

* Corresponding author: dongj@ucmail.uc.edu (J.D.)

SUPPORTING INFORMATION

Fig. S1. Porous PVDF film stability in the highly oxidizing and acidic solution of 2M $(VO_2)_2SO_4$ (V^{5+}) + 2M H_2SO_4 (i.e., high concentration catholyte of vanadium RFB): (a) fresh sample, (b) sample after 6-month treatment in the solution, and (c) sample weight as a function of time in solution,

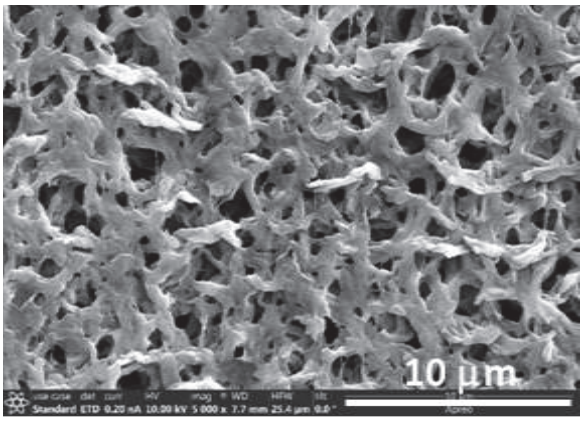

(a)

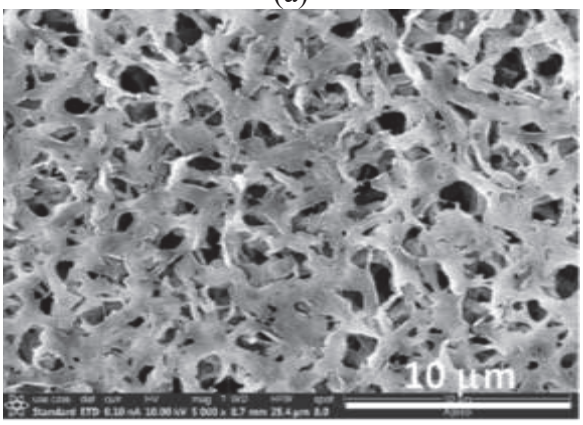

(b)

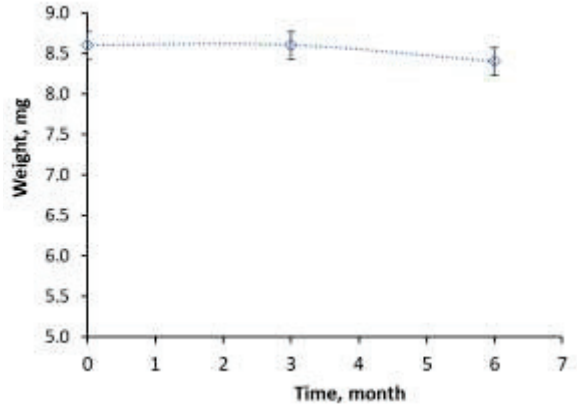

(c)

Fig. S2. (a) Photograph of the vacuum-assisted filtration coating apparatus and (b) schematic showing the self-repairing mechanism of the filtration coating process [**21**].

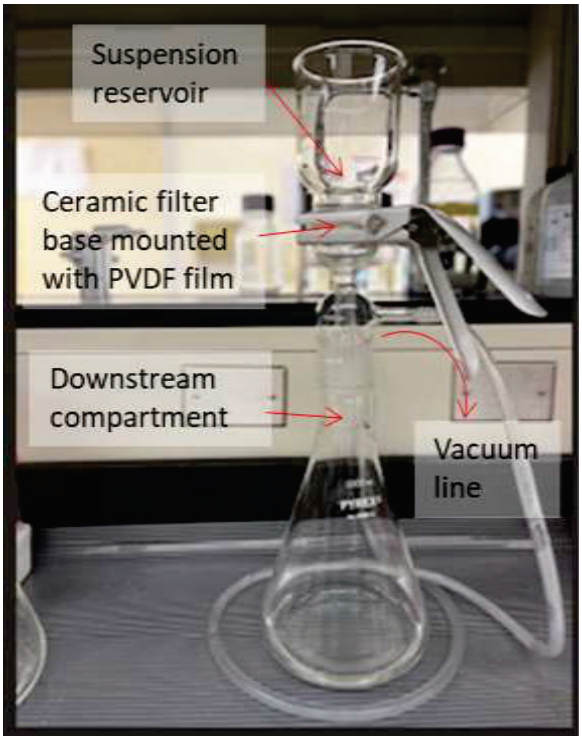

(a)

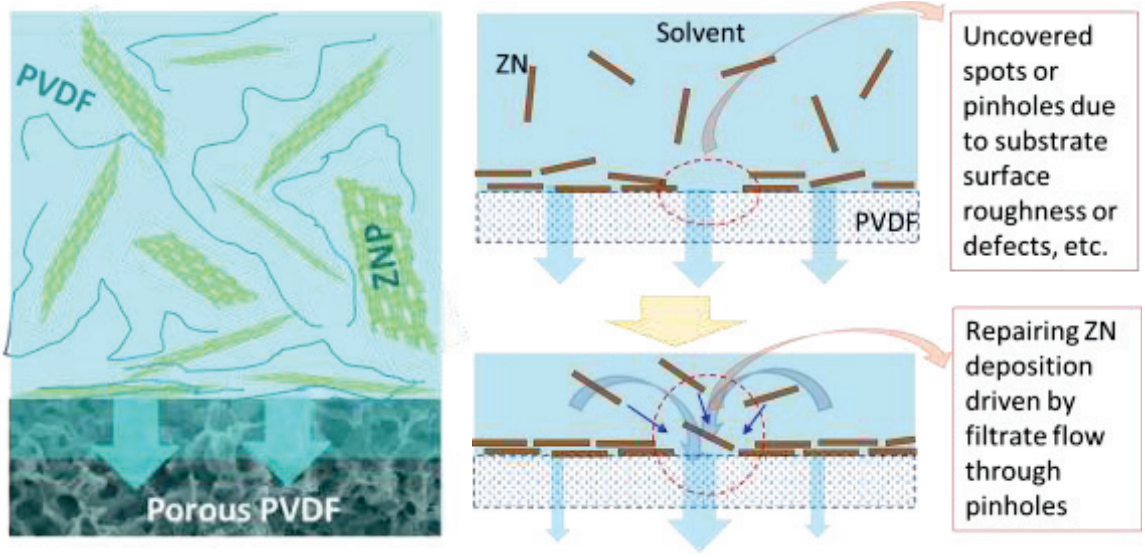

(b)

Fig. S3. Photograph of the RFB single cell used for measurements of EIS, RFB charge-discharge, and RFB polarization curves.

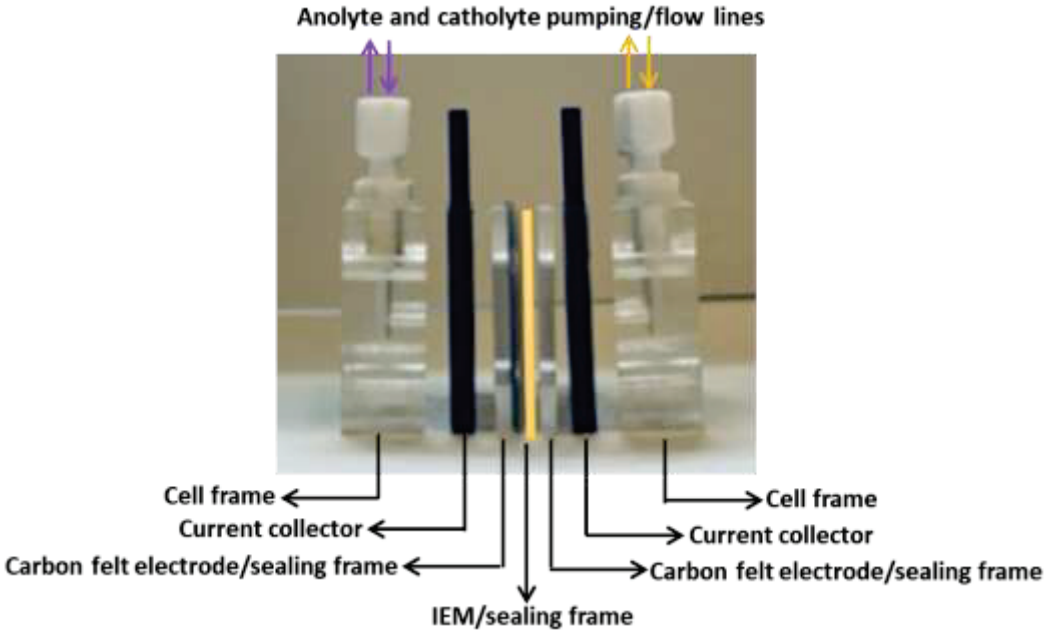

Fig. S4. Zeolite samples and pore size distributions: (a) SEM image of the flower-like ZN assemblies after SDA removal by calcination in air at 550ºC for 6 h, (b) regular brick-shaped silicalite crystals, and (c) pore size distributions of the activated ZN assemblies and regular crystals.

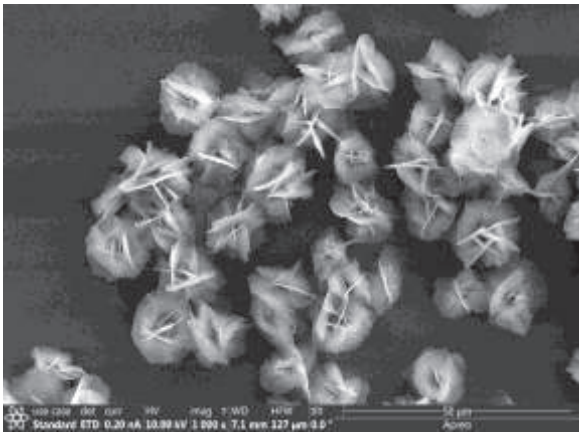

(a)

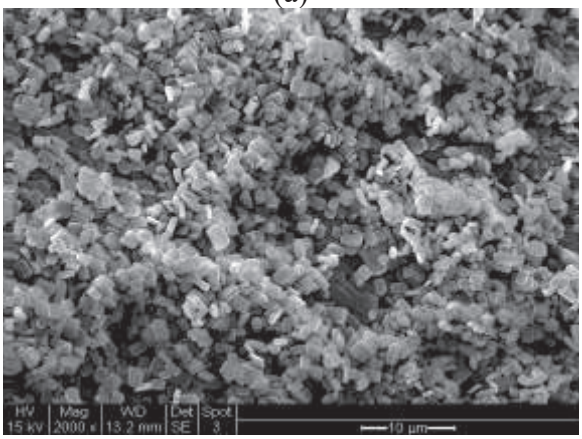

(b)

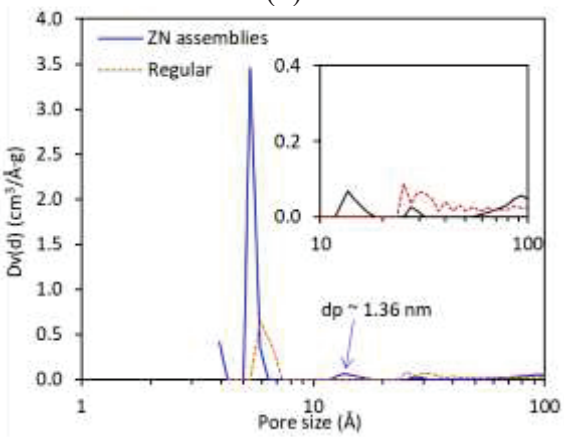

(c)

Fig. S5. ZNPT-PVDF membranes from suspensions with ZNP contents that were too low or too high to avoid defect formation: (a) and (b) SEM picture of the ZNPT membrane from suspension containing 0.01wt% ZNPs and results of its ion diffusion test, respectively; and (c) and (d) SEM picture of the membrane from suspension with 0.06wt% ZNPs and results of its ion diffusion test, respectively. The same amounts of suspension (3.5 mL) were used for total filtration membrane coating and thus the thickness was expected to be ~250 nm for the former and ~1.5 μm for the latter. The J_{H^+}, J_{V^4}, and $\alpha_{H/V}$ estimated from mixture permeation data in (b) and (d) are summarized and compared with the ZNPT-PVDF membrane from suspension containing 0.02wt% ZNPs in Table S1.

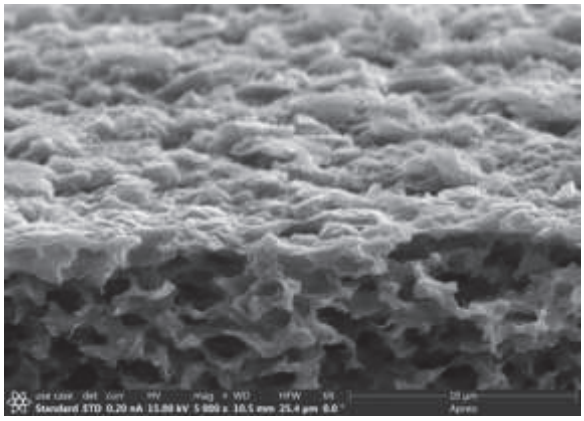

(a)

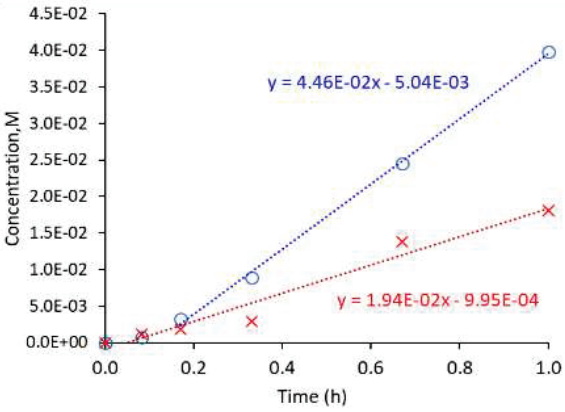

(b)

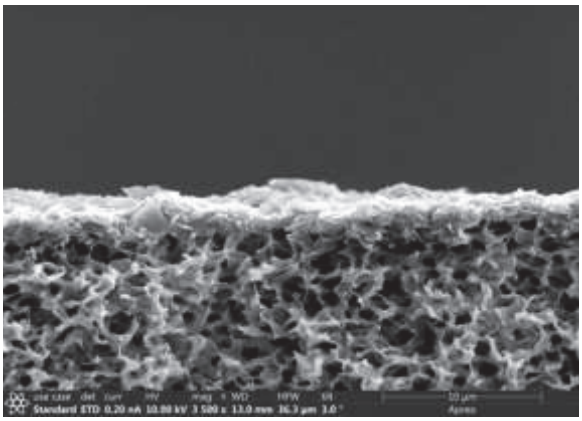

(c)

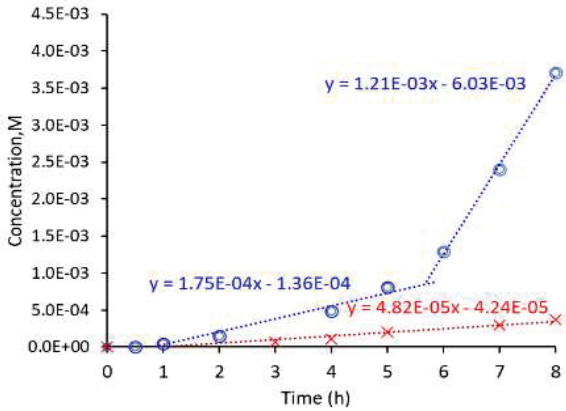

(d)

Fig. S6. SEM images of the NZ-ZNPT-PVDF synthesized under same conditions as used for ZNPT-PVDF membrane preparation: (a) cross-section and (b) surface.

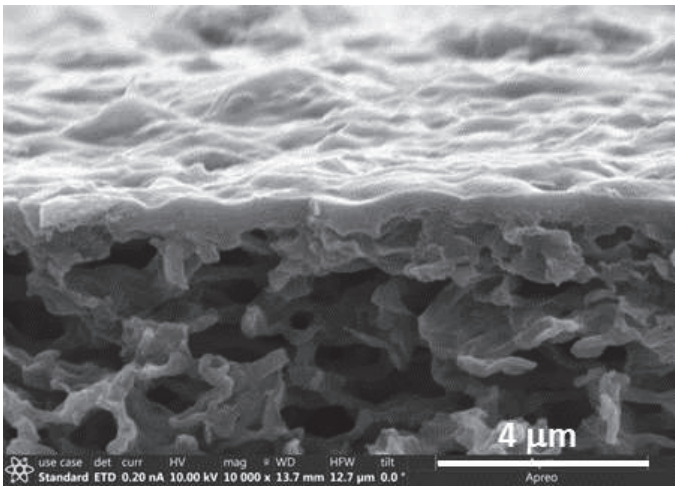

(a)

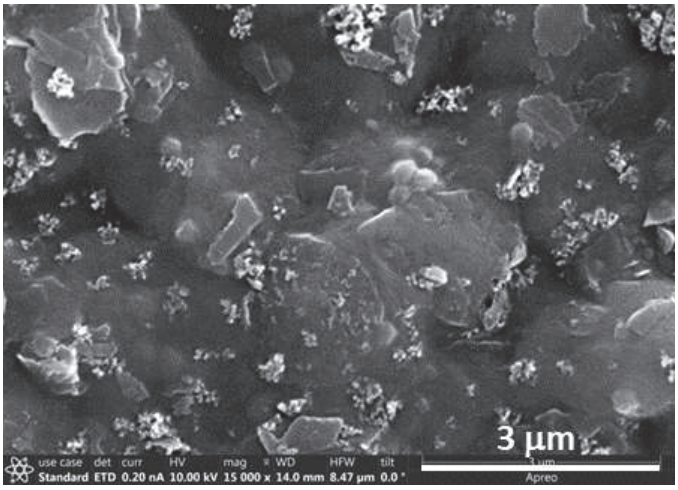

(b)

Fig. S7. UV adsorption spectra for various VO^{2+} concentrations in 1 M MgSO4 solution for calibration. The concentrations of VO^{2+} in the permeate sides of the highly selective ZNPT-PVDF were well below 10^{-4} M in the first 3 h that caused large measurement errors. Thus, the data after 4 h were used for determining VO^{2+} flux. The data of late period were also appropriate for selectivity calculation with the linear segment of H^{+} concentration trend.

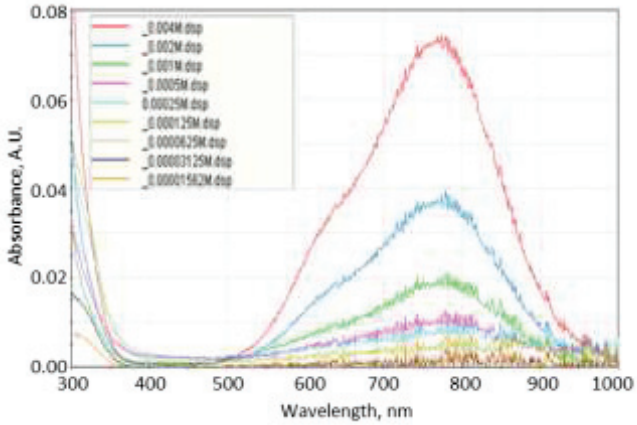

Fig. S8. Transient ion diffusion/permeation results for operations with the ZNPT layer facing the feed (4/7M $VOSO_4$ + 4/7M H_2SO_4) and the sweep solution on permeation side (1M $MgSO_4$), respectively. The membrane orientation appeared to have no significant impacts on the ion selectivity and fluxes when stabilized.

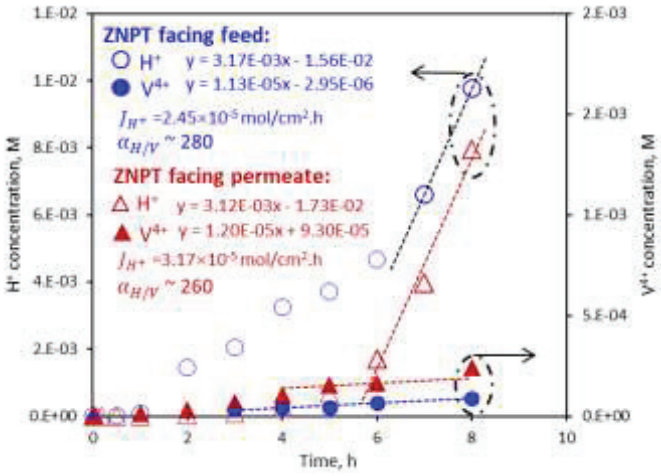

Fig. S9. Results of transient ion permeation on a ZNPT-PVDF membrane presoaked with 2 M H_2SO_4 solution in comparison with that on the water-soaked ZNPT-PVDF in Fig. 5: (a) time-dependencies of ion concentrations for H_2SO_4-soaked membrane and water-soaked membrane, respectively, (b) linearly fitted time-dependences for H^+ and V^{4+} concentrations in stabilized stages, (c) time-dependencies of H^+ concentrations in the initial periods of diffusion showing the H_2SO_4-soaked membrane causing much earlier onset of H^+ concentration increase as compared to the water-soaked membrane, and (d) time-dependencies of V^{4+} (VO^{2+}) concentrations in the initial periods showing delayed transitional increases of V^{4+} concentrations for both membranes. The one set of V^{4+} concentration increase for the H_2SO_4-soaked membrane appeared to be delayed for longer time. This could be attributed to its higher selectivity ($\alpha_{H/V} \sim 480$) and lower V^{4+} flux as well as the large uncertainty of UV spectroscopic measurements below 2×10^{-5} M (Fig. S7).

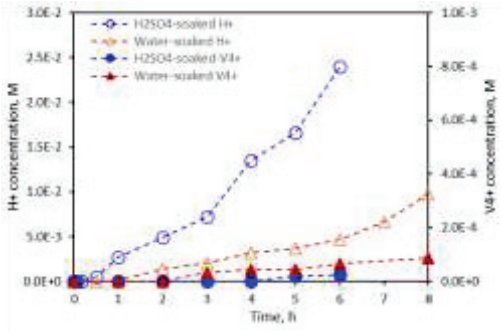

(a)

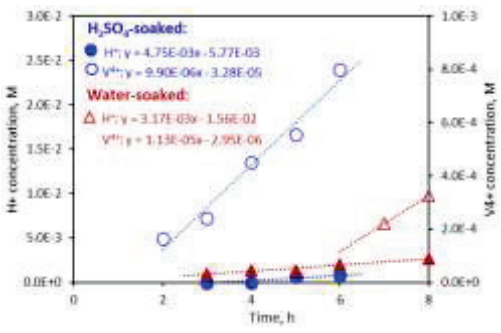

(b)

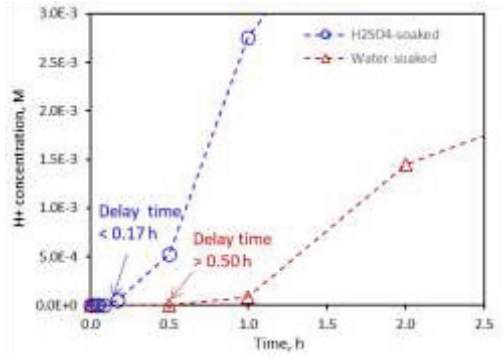

(c)

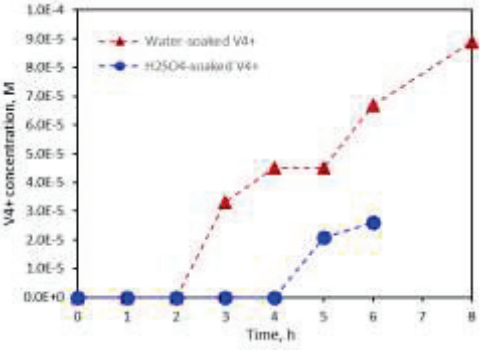

(d)

Fig. S10. Use of polarization curves for RFB and IEM property analyses: the linear sections of the polarization curves for estimating the *ASR* for the ZNPT-PVDF and Nafion117 membrane under RFB operation conditions.

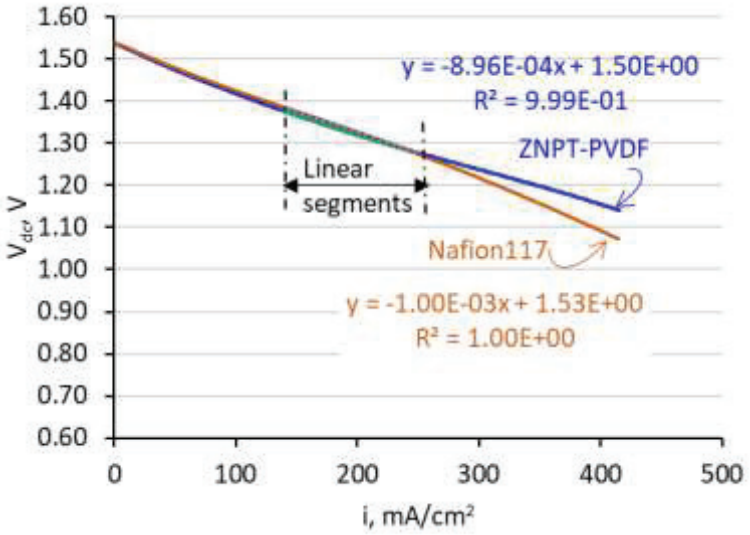

Fig. S11. SEM images of the ZNPT-PVDF membrane after RFB charge-discharge operations: (a) cross-section, and (b) surface.

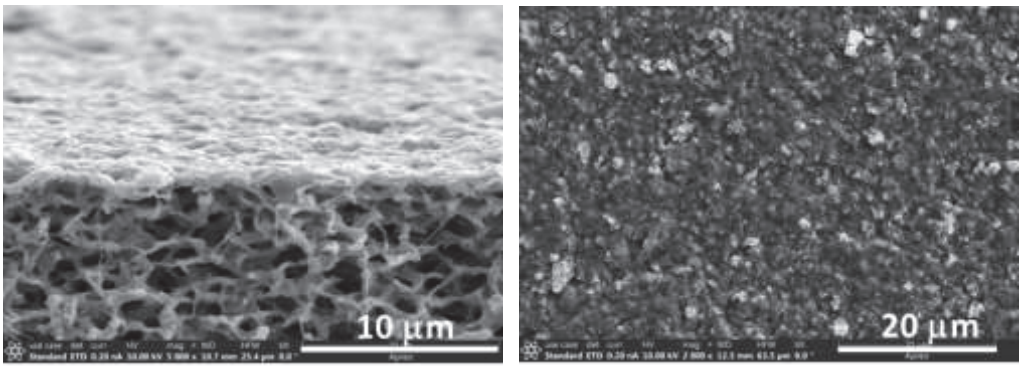

(a) (b)

Table S1. The ion fluxes (J_{H^+} and $J_{V^{4+}}$) and proton selectivity $\alpha_{H/V}$ for ZNPT membranes in Fig. S5 made from ZNP suspensions of various ZNP contents

ZNP content in suspension, wt.%	J_{H^+}, *mol/cm²·h*	$J_{V^{4+}}$, *mol/cm²·h*	$\alpha_{H/V}$	$\alpha'_{H/V}$*
0.01	6.19E-04	2.69E-04	2.3	1.2
0.02	4.40E-05	1.57E-07	280.5	140
0.06	1.68E-05	6.69E-07	25.1	13.0

$$* \alpha'_{H/V} = \frac{J_{H^+}/(C_{f,H^+} - C_{p,H^+})}{J_{V^{4+}}/(C_{f,V^{4+}} - C_{p,V^{4+}})}$$

Table S2. Ion fluxes and proton permeation selectivity for various membrane layers in Fig. 5.

Membrane layer	δ_m, μm	J_i, mol/h·cm^2		$\alpha_{H/V}$	$\alpha'_{H/V}$*
		$i = H^+$	$i = V^{4+}$		
Bare PVDF	125	4.64E-03	2.58E-03	1.8	0.9
NA-ZNPT	0.50	3.35E-06	7.40E-07	4.5	2.3
ZNPT: stage 3	0.50	2.54E-05	9.04E-08	280.5	140
ZNPT: stage 2	0.50	7.08E-06	9.04E-08	78.3	39
ZNPT: stage 1	0.50	5.58E-07	9.04E-08	6.2	3.1
Nafion117®	183	1.04E-04	4.85E-06	21.5	10.8

$$* \alpha'_{H/V} = \frac{J_{H^+}/(C_{f,H^+} - C_{p,H^+})}{J_{V^{4+}}/(C_{f,V^{4+}} - C_{p,V^{4+}})}$$